

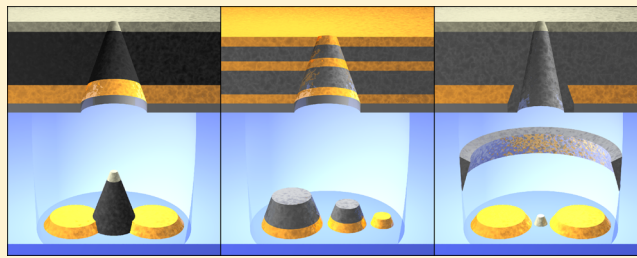
# Shrinking-Hole Colloidal Lithography: Self-Aligned Nanofabrication of Complex Plasmonic Nanoantennas

Svetlana Syrenova, Carl Wadell, and Christoph Langhammer\*

Department of Applied Physics, Chalmers University of Technology, 412 96 Göteborg, Sweden

## Supporting Information

**ABSTRACT:** Plasmonic nanoantennas create locally strongly enhanced electric fields in so-called hot spots. To place a relevant nanoobject with high accuracy in such a hot spot is crucial to fully capitalize on the potential of nanoantennas to control, detect, and enhance processes at the nanoscale. With state-of-the-art nanofabrication, in particular when several materials are to be used, small gaps between antenna elements are sought, and large surface areas are to be patterned, this is a grand challenge. Here we introduce self-aligned, bottom-up and self-assembly based Shrinking-Hole Colloidal Lithography, which provides (i) unique control of the size and position of subsequently deposited particles forming the nanoantenna itself, and (ii) allows delivery of nanoobjects consisting of a material of choice to the antenna hot spot, all in a single lithography step and, if desired, uniformly covering several square centimeters of surface. We illustrate the functionality of SHCL nanoantenna arrangements by (i) an optical hydrogen sensor exploiting the polarization dependent sensitivity of an Au–Pd nanoantenna ensemble; and (ii) single particle hydrogen sensing with an Au dimer nanoantenna with a small Pd nanoparticle in the hot spot.



**KEYWORDS:** Hole-mask colloidal lithography, localized surface plasmon resonance, nanoantenna, single particle spectroscopy, palladium, hydrogen sensing

The fascinating ability of plasmon-resonant metallic nanostructures, plasmonic nanoantennas,<sup>1</sup> to strongly localize and enhance electromagnetic fields in so-called hot spots<sup>2–4</sup> has placed them at the focus of envisioned photonics technologies and a plethora of research endeavors. The hot spot usually corresponds to the edges, sharp corners, or tips of monomer structures, and in case of coupled multimer arrangements, to the antenna junctions, that is, the gap(s) between two or several antenna elements. Typically, such nanoantennas have so far been made from a single material, usually Au or Ag due to their favorable plasmonic properties. For numerous envisioned applications, however, it is of critical importance to be able to place one or several well-defined nanoobject(s), consisting of another material than the antenna itself, in the hot spot(s) of the antenna. For example, such arrangements would be of high value for in situ spectroscopy for materials science applications,<sup>5</sup> enhanced (photo-) catalysis,<sup>6–9</sup> and chemosensing<sup>10</sup> but also, as shown recently, in loaded nanoantennas to tune the antenna resonance and impedance bandwidths in optical nanocircuits.<sup>11,12</sup> However, the efficient fabrication of such polymaterial plasmonic nanoantenna arrangements is today in particular on surface areas exceeding a few tens of square micrometers, a grand experimental/nanofabrication challenge. The latter imperatively needs to be addressed if any of the envisioned applications are to take the step from the laboratory to industry and thus to useful products.

To date, electron beam lithography (EBL) and focused ion beam (FIB) milling are the nanofabrication workhorses in nanoscience and technology in general, and in plasmonic nanoantenna-related research in particular. These methods have been widely used for the fabrication of structures like bowtie<sup>13–15</sup> and diabolo<sup>16</sup> nanoantennas, as well as nanorod,<sup>12,17,18</sup> nanodisk,<sup>11,19,20</sup> nanoblock,<sup>21</sup> nanoring,<sup>22,23</sup> and circular<sup>24</sup> or rectangular<sup>25</sup> hole pairs/dimers. They are highly efficient and versatile as long as only small areas are to be patterned and as homomaterial structures are to be crafted. However, as soon as more complex nanoantenna arrangements with elements/features smaller than 20–30 nm are to be made, the limits of these techniques are reached quickly, both in terms of resolution and alignment accuracy. The latter is particularly important when (i) more than one material is to be used, (ii) several exposure–development–material deposition sequences are necessary, and (iii) small gaps between antenna elements are sought to maximize local field enhancement in the hot spot. Moreover, electron and ion beam-based nanofabrication strategies are serial processes where each nanostructure is “written” individually. This renders these techniques slow and expensive, as well as highly inefficient if larger areas (cm<sup>2</sup> or more) are to be patterned.

**Received:** February 9, 2014

**Revised:** March 21, 2014

**Published:** April 3, 2014

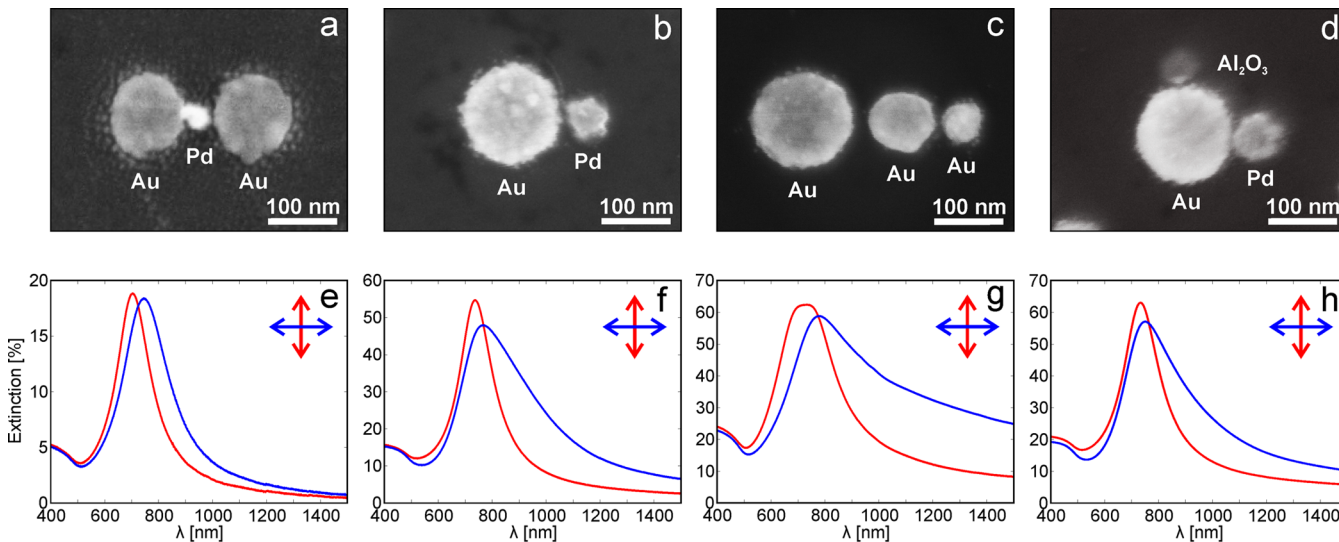


**Figure 1.** Selection of complex polymaterial nanoantennas made by SHCL (a–d) with corresponding polarization-dependent far-field ensemble extinction spectra (e–h). The red and blue spectra for each structure correspond to two incident light polarizations indicated by the arrows. (a) Au nanodisk dimer with small Pd nanoparticle in the gap. The structure was made with the sacrificial C cone strategy. (b) Au–Pd nanodisk heterodimer. This structure was made using the sacrificial Cr cone approach. (c) Self-similar Au disk nanoantenna, as predicted by Li et al.<sup>39</sup> This structure was made using the sacrificial Cr cone strategy. (d) Au nanoantenna featuring a Pd and Al<sub>2</sub>O<sub>3</sub> nanoparticle on each side. This structure nicely illustrates the possibility offered by SHCL to deposit several particles around a nanoantenna at different positions and to make them from different materials. This structure was made using the sacrificial Cr cone strategy.

In this work, we present three versatile self-assembly based “Shrinking-Hole Colloidal Lithography” (SHCL) nanofabrication strategies for the efficient fabrication of complex plasmonic nanoantenna structures (in focus here), as well as other advanced nanoarchitectures. The SHCL approach is characterized by two generic advantages. The first one, as we will show below, is its inherent self-alignment, which makes it possible to produce antenna elements with small gaps that consist of different materials with a superior level of control and accuracy in a single lithography step. Specifically, SHCL-nanoarchitectures can consist of several elements with continuously tunable sizes and gaps and, if desired, be made from different metals, semiconductors, and insulators on a support of choice (e.g., conducting or nonconducting). Moreover, SHCL allows the accurate positioning of small (<10 nm) nanoobjects in, for example, the hot spot of a plasmonic nanoantenna. The key beyond-state-of-the-art step introduced here that makes this possible, compared to the “traditional” hole-mask colloidal lithography (HCL<sup>26</sup>) method, is the use of sacrificial nanostructures like chromium (Cr) and carbon (C) nanocones and a Cr nanofunnel, which allow both accurate lateral positioning and size control down to the sub-10 nm range. The second generic advantage of SHCL, common to most colloidal lithography approaches,<sup>27</sup> is that it is self-assembly based, as it exploits a colloidal lithography strategy to produce the initial mask. This makes it conveniently possible to homogeneously cover several square centimeters of a desired surface with complex nanostructures, as we show below. We note also that the presented concepts of exploiting sacrificial nanostructures for the self-aligned transfer and size/position control of small nano-objects to nanoantenna hot spots are generic. In other words, alternative methods than colloidal lithography-based ones, for example, EBL or FIB, can equally well be used to produce the hole-mask that constitutes the “starting point” of the new concepts introduced here and discussed in detail below.

In the second part of this paper, to demonstrate the functionality of antenna arrangements made by SHCL both at the ensemble and single particle level, we present two specific application examples. The first one is an all-optical hydrogen sensor exploiting the polarization dependent sensitivity of an Au–Pd dimer nanoantenna ensemble. The second example is the single particle hydrogen sensing capability of an Au dimer nanoantenna with a small Pd nanoparticle in the hot spot of the antenna gap. We choose hydrogen sensing as our model system because (i) hydride formation in Pd is a well-understood and reversible process,<sup>28</sup> (ii) it challenges the sensitivity of plasmonic sensors at low H<sub>2</sub> concentrations, and (iii) it nicely illustrates that our nanofabrication methods neither contaminate nor alter the intrinsic properties of the materials used. In the present case of Pd, this means that its catalytic activity (hydrogen dissociation on the surface) and hydride forming capability (in the bulk) are retained. Moreover, both direct<sup>29–32</sup> and indirect<sup>10,33–38</sup> nanoplasmonic hydrogen sensing are well-established concepts in the field that have been introduced by us and demonstrated in different versions by other groups. This is another reason why we choose this particular concept to demonstrate the functionality of complex nanoantenna arrangements made by SHCL.

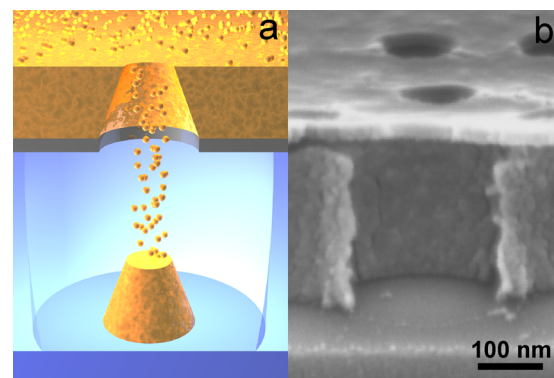
We now start out with presenting a representative selection of structures that can be made by SHCL and assess their optical response at the ensemble level, that is, we measure polarization dependent optical extinction spectra on a sample area of ca. 25 mm<sup>2</sup>. This emphasizes one of the strengths of our method, namely the possibility to uniformly pattern large sample areas with a high coverage of well-defined nanostructures with the same orientation. We also emphasize that other material combinations (metals, semiconductors, insulators) than the ones shown in the below examples are equally feasible.

Figure 1a shows an Au dimer antenna with a ca. 40 nm gap and with a Pd nanoparticle ( $D \approx 30$  nm) in the gap (hot spot). A clear dependence of the optical response for parallel and

perpendicular polarization with respect to the dimer axis is seen due to the near-field coupling between the antenna and the Pd particle in the case of parallel-polarized light. Figure 1b shows an Au–Pd heterodimer nanoantenna featuring a smaller Pd nanoparticle adjacent to a large Au disk. Also here we observe a strong polarization dependence of the far-field response, indicating the strong coupling between the Au and Pd elements. Figure 1c shows a nanoantenna featuring three Au disk elements with decreasing diameter in a row. Such “self-similar” antennas, as predicted by Li et al.,<sup>39</sup> exhibit hot spots between the two smaller antenna elements with greatly enhanced field intensities compared to, for instance, a dimer structure due to a cascaded enhancement, that is, the largest particle collects the light and the smallest localizes the field. Such self-similar antenna structures have previously been produced by DNA templating<sup>40</sup> or by “picking up” nanospheres one by one using a SNOM tip.<sup>41</sup> In the latter case, they have shown the ability to greatly enhance fluorescence of single molecules. Figure 1d shows an arrangement of a central Au nanoantenna with a small Pd particle placed on one side and an Al<sub>2</sub>O<sub>3</sub> particle on the other. This nicely illustrates the possibility offered by SHCL to (i) deposit several particles around a nanoantenna at different positions and (ii) make them from different materials. The polarization-dependent far-field response shows a broadened and slightly damped resonance when the antenna couples with the (lossy) Pd particle, whereas the narrow line shape is retained when the light is polarized in the direction of the (dielectric) Al<sub>2</sub>O<sub>3</sub> particle.

We now turn to a detailed discussion of the three SHCL strategies that were used to make the structures shown in Figure 1 and used in the examples below. They all build on the generic HCL<sup>26</sup> nanofabrication approach (whose initial nine fabrication steps are summarized in the Methods Section and in Supporting Information Figure S1) onto which we have implemented three different variations of a novel critical step to vastly enhance the versatility of the method. This step constructively exploits the effect of a “shrinking hole” in the HCL mask upon material deposition by utilizing the growth of sacrificial nanostructures, hence the name Shrinking-Hole Colloidal Lithography. In brief, the hole shrinking effect arises from the fact that as material is deposited through the hole-mask (which was fabricated in the initial 9 standard HCL steps) material is also continuously built up at the rim of the hole as schematically illustrated in Figure 2. This causes the hole to shrink continuously at a constant rate during material deposition. The shrinking rate depends on the specifics of the deposition process and the deposited material. If exploited carefully, as we will show, this effect provides unique possibilities for the self-aligned crafting of complex multi-material nanostructures on a surface with a very high level of control of the size and position of the constituent elements. Depending on the specifics of the targeted application and material combinations of the arrangement, the sacrificial nanostructure used for SHCL nanofabrication can constitute (i) a carbon (C) nanocone, (ii) a chromium (Cr) nanocone, or (iii) a Cr nanofunnel.

To illustrate the first variation of the SHCL approach we use an Au nanodisk dimer as initial nanoantenna structure, and a sacrificial C nanocone as the sacrificial particle transfer structure (Figure 3). The Au nanodisk dimer is fabricated by executing fabrication steps 1–9 of standard HCL described in the Methods Section. Therefore, here, we start our detailed description at (Step 10). C is e-beam evaporated at normal



**Figure 2.** (a) Sketch of the “shrinking hole” process during evaporation through a hole-mask. During the deposition, material is continuously building up not only on top of the mask layer but, critically, also at the rim of the holes in the evaporation mask, causing the hole to shrink. This continuous closing of the hole gives rise to a conical shape of the formed nanostructures. If exploited carefully, as we demonstrate here, this effect facilitates the self-aligned fabrication of complex nanostructures with a high level of control of both size and lateral positioning of nanoparticles on the surface exposed below the hole-mask. (b) Tilted cross-section SEM image of hole-mask after plasma etching. Note the under-etching of the PMMA layer down to the support layer.

incidence through the hole-mask and forms a cone due to the successive shrinking of the nanoholes of the mask upon C deposition onto the rims of the hole. The rate and the thickness during C evaporation are carefully controlled to make sure that the holes in the mask do not close completely in order to provide enough space for later deposition of the material that will form the particle to be delivered to the antenna hot spot (see Supporting Information Figures S2 and S3). (Step 11) The particle material (here, Pd) is deposited directly after C at normal incidence through the small hole that is left from the previous step. In such a way, it forms a small particle on top of the sacrificial C cone structure (Figure 3a). The diameter of the particle is controlled by the thickness of the evaporated C layer (cone height). Evaporating C and/or particle material at a small angle from the normal will, additionally, result in tunable lateral particle position (Figure 3 e,f vs g,h). (Step 12) The sample is placed in acetone to dissolve the PMMA layer in a lift-off together with all the excess material on top. (Step 13) The sacrificial C cone is etched away in mild oxygen plasma. The oxygen radicals thereby attack the C cone uniformly from all directions, such that the particle is delivered into the gap of the gold dimer as illustrated in the sequence of SEM images in Figure 3a–d. This first approach to use a C cone as the sacrificial nanostructure works well for delivering the particle of interest into the gap of the nanodisk dimer. The drawback (or equally advantage if an oxide particle is to be delivered) of this method is that oxygen plasma etching, which is used to remove the C, also may oxidize the particle or nanoantenna material (for example when Ag is used).

In order to eliminate the above-mentioned issues related to unwanted oxidation, we introduce Cr as alternative sacrificial nanostructure material in a second version of SHCL. To illustrate this approach, instead of an Au nanodisk dimer, we use a single Au nanodisk as the nanoantenna structure. As shown in Figure 4a, here Cr is deposited at normal incidence instead of C to form the sacrificial cone structure during step 10. In this way the diameter of the hole in the mask, and thus

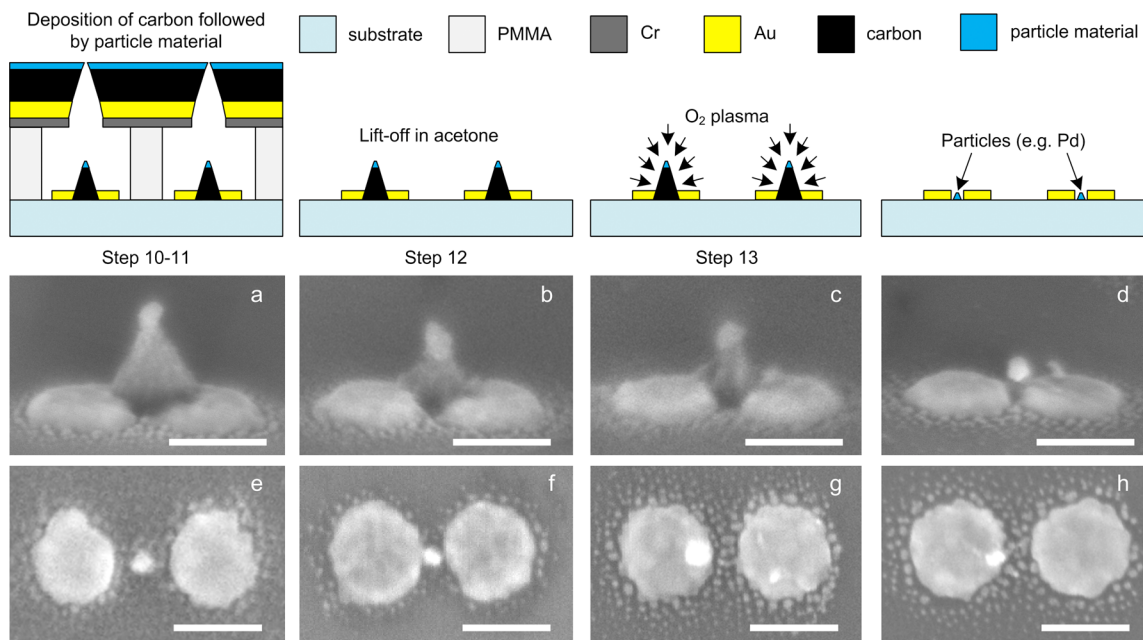


**Figure 3.** Schematic illustration of the first SHCL nanofabrication strategy used here for placing a small Pd particle in the gap of an Au nanodisk dimer by using a C cone as the sacrificial particle transfer structure. (a–d) Seventy degree tilted SEM images of a sample made on a Si wafer substrate after 1, 2, 3, and 4 min in oxygen plasma, respectively. Clearly, the homogeneous removal of the sacrificial C structure by the oxygen plasma is seen with the consequent “delivery” of the Pd particle in the antenna gap. (e,f) SEM images of Au nanodisk dimers ( $D_{\text{Au}} = 105 \text{ nm}$ ) with different gap sizes (60 and 23 nm) and with a Pd particle with diameter  $D_{\text{Pd}} = 20 \text{ nm}$  in the gap. (g,h) SEM images of Au nanodisk dimers with a gap of 30 nm and with small Pd particles with two different sizes (21 and 10 nm) placed at different lateral positions and in the gap. The scale bar in all SEM images is 100 nm.

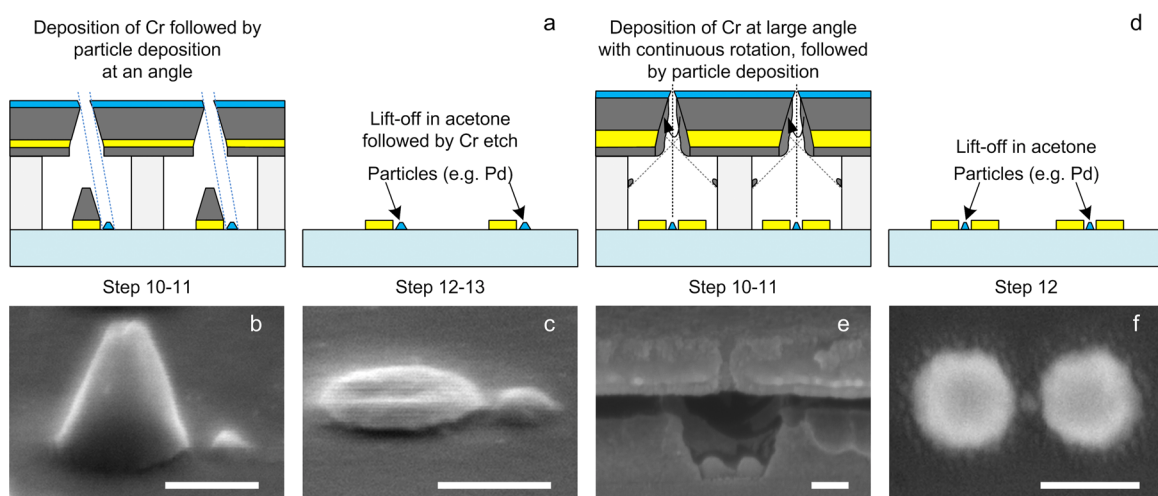


**Figure 4.** Schematic illustrations of the second (Cr-cone, left) and third (Cr-funnel, right) SHCL nanofabrication strategies used here for placing a Pd nanoparticle next to an Au nanodisk antenna or in the gap/hot spot of an Au dimer, respectively. (a) Sacrificial Cr-cone strategy: Cr is deposited at normal incidence to shrink the hole in the mask and forms a cone on top of the Au antenna. When the desired hole-size has been reached, the second particle (here Pd) is deposited through the mask at a small angle from the normal. After lift-off to remove the mask, the sacrificial Cr cone is removed using a liquid Cr etch. (b) SEM image of a Cr cone with an Au nanodisk underneath and a small Pd particle next to it. (c) SEM image of an Au nanodisk ( $D_{\text{Au}} = 140 \text{ nm}$ ) and smaller Pd particle ( $D_{\text{Pd}} = 50 \text{ nm}$ ,  $t_{\text{Pd}} = 20 \text{ nm}$ ) next to it after the Cr etch step. (d) Sacrificial Cr-funnel strategy: Cr is deposited at a large angle from the normal with continuous sample rotation to form a funnel while shrinking the hole in the mask. In this way the Cr is deposited only onto the mask and onto the walls of the (underetched) PMMA resist layer in the hole, that is, no Cr is deposited onto the sample surface. Therefore, all the excess material can be removed directly during the final lift-off and no reactive or wet etch is required. (e) SEM image of a sample cross-section before lift-off. The sample features Ag nanodisk dimers ( $D_{\text{Ag}} = 80 \text{ nm}$ , thickness  $t_{\text{Ag}} = 40 \text{ nm}$ ) with a Pd particle in the gap. (f) Representative SEM image of a Au nanodisk dimer with a Pd particle ( $D_{\text{Pd}} = 17 \text{ nm}$ ,  $t_{\text{Pd}} = 10 \text{ nm}$ ) in the gap (25 nm) fabricated using the Cr funnel approach. The scale bar in all SEM images is 100 nm.

the size of the final nanoparticle, can again be finely adjusted via the hole-closing effect mentioned above (see Supporting Information Figure S4 for more information). (Step 11) The material to form the second particle is deposited at an angle

from the normal (to avoid deposition onto the Cr cone) through the tuned hole-mask to be delivered to the close vicinity of the antenna disk (Figure 4b). Tuning of the particle evaporation angle will yield various particle positions relative to

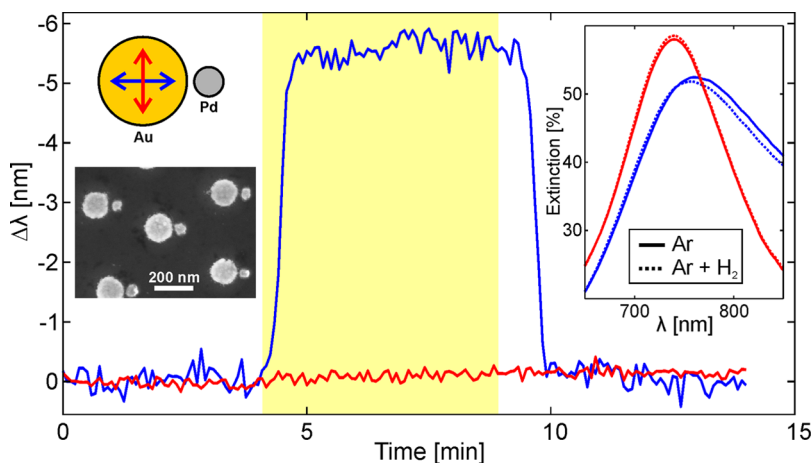


**Figure 5.** Polarization-dependent hydrogen sensing with Au–Pd nanoantennas fabricated using the Cr cone approach. The Pd particle can absorb hydrogen and forms a hydride,  $\text{PdH}_{\nu}$ , above a critical hydrogen pressure. This process changes its dielectric properties as well as its volume, which is “sensed” by the Au element via near-field coupling and gives rise to a spectral shift of the antenna resonance. For parallel polarization (blue curve) the peak shifts to shorter wavelengths as hydrogen is absorbed in the Pd antenna element during a 4% hydrogen pulse (yellow shaded area), whereas no response is recorded for perpendicular polarization (red curve). The corresponding extinction spectra for the two polarizations in pure Ar (solid lines) and in 4%  $\text{H}_2$  in Ar (dashed lines) are shown as inset together with an SEM picture of the structures.

the Au nanodisk. Alternatively, if, for example, a nanodisk dimer were the initial antenna structure, one would deposit the Cr cone at an angle and then the particle material at normal incidence to deliver the particle to the dimer hot spot. (Step 12) The PMMA layer with excess material on top is removed by lift-off in acetone. (Step 13) The Cr cone is removed by dipping the sample in a liquid Cr etch, leaving only the antenna with a particle in the hot spot on the surface (Figure 4c).

This second SHCL approach, which exploits a sacrificial Cr cone, is very efficient and straightforward to implement. However, also in this case there are a number of limitations in the range of materials that can be used for nanoantenna structure and particle material, dictated by the compatibility with Cr etch. Moreover, concerns may arise about possible contamination of the sample (e.g., when catalytic/chemical processes on the formed particle are of interest) from the wet etch step.

As a solution to overcome all these concerns, we present a third SHCL strategy that as the only additional requirement relies on an e-beam evaporation system that features sample tilt and rotation simultaneously during deposition. In this way, we are able to eliminate any etching step by again employing Cr to grow a sacrificial structure to tune the diameter of the hole in the mask. Now, however, it is deposited onto the hole-mask at a large angle ( $\beta$ ) and with continuous rotation of the sample. In this way, owing to the significant under-etching of the PMMA in the hole-mask, a Cr funnel structure is grown around the nanoantenna in the hole (Figure 4e). The Cr is deposited until the hole in the mask decreases sufficiently for the desired diameter of the particle to be delivered to the antenna (step 10) and then the particle material is deposited through the remaining hole either orthogonally to the surface or at an angle to control the lateral position with respect to the nanoantenna (step 11). Given that the angle of Cr evaporation is chosen appropriately (which exact angle to use depends on the size of the initial hole of the hole-mask and on the PMMA thickness, here,  $\beta = 30^\circ$ ), it will be deposited only on the walls of the PMMA layer (i.e., not onto the sample surface itself), such that all the sacrificial material can be removed directly during the lift-off in acetone (step 12), and without having to

use the Cr etch at a later step. Hence, any incompatibilities with oxidation-sensitive or non-wet-etch-resistant materials are completely eliminated, as well as the risk for contamination. At the same time the impressive flexibility to build complex polymaterial nanoantenna structures in a completely self-aligned way is retained.

As a general remark, it is important to note that the antenna arrangements obtained by all three SHCL versions are quasi-randomly distributed on the surface (no long-range order) according to the patterns formed in the colloidal self-assembly step (see Supporting Information Figures S6 and S7 for a representative overview SEM image). As for the similarity of individual antennas in an array, the latter is to a large extent determined by the polydispersity of the utilized colloidal spheres. The distribution in sizes is directly reflected in the distribution of sizes of the antennas and its elements, and thus the accuracy with which individual elements can be positioned. Finally it is also important to briefly address the achievable maximum depth of the undercut in PMMA since it determines the maximal lateral dimensions of the nanostructures. The undercut depends on etching time, PMMA thickness, size of PS particles used to make the hole-mask, but also on the coverage of the PS particles. The etching is limited by the fact that some critical amount of PMMA needs to remain after etching in order to support the mask during further processing. In a case when high concentration of PS particles is used to achieve high nanoantenna coverage on the surface, excessive etching will result in the mask collapsing on the substrate. For lower concentrations of PS particles (i.e., for single particle studies as shown below), where the corresponding coverage on the sample surface will be very low, in principle, the etching can be done for much longer time to achieve massive undercuts that would allow large lateral antenna dimensions.

In the second part of this paper, we will now present a number of nanoantenna arrangements prepared with SHCL and show, on two specific examples, what functionality that can be achieved. As the first example, we demonstrate an all-optical hydrogen sensor by exploiting the structure introduced in Figure 1b, that is, an amorphous array (covering  $100 \text{ mm}^2$ ) of large Au disks, acting as the sensing element, with an adjacent

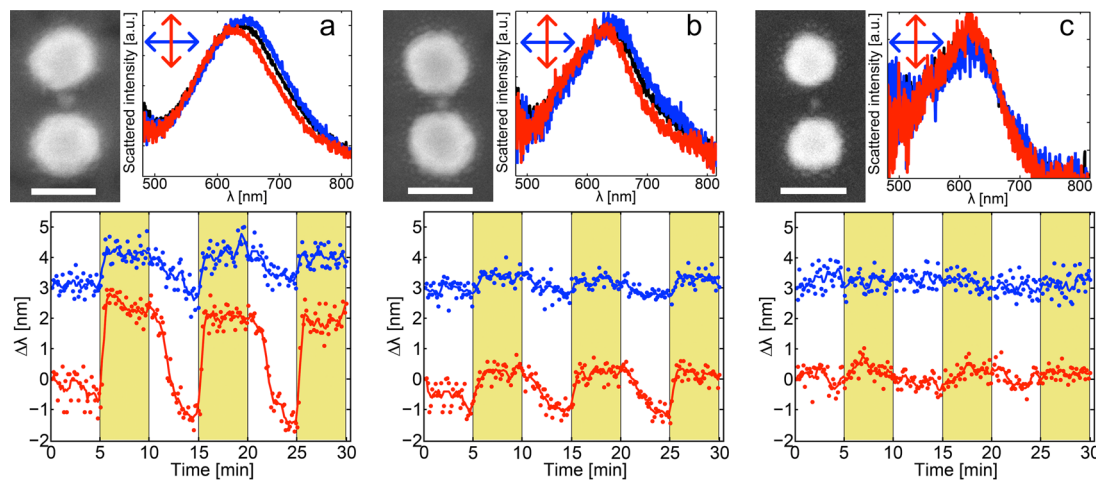


**Figure 6.** SEM images of three Au dimer antenna structures with a small Pd nanoparticle in the gap fabricated using the Cr funnel approach. The images are shown together with the corresponding polarization dependent single particle scattering spectra (to the right) and polarization dependent single particle hydrogen sensing measurements (below). As above, the small Pd nanoparticle in the antenna gap can absorb hydrogen in a hydride phase, which alters its dielectric properties and volume. Due to the positioning of the Pd particle in the antenna hot spot, the hydrogen sorption process is “sensed” efficiently by the Au elements despite the small size of the Pd particle. (a) Dimer with  $D_{\text{Au}} \sim 105$  nm,  $D_{\text{Pd}} \sim 26$  nm, dimer gap size  $G \sim 34$  nm. (b)  $D_{\text{Au}} \sim 100$  nm,  $D_{\text{Pd}} \sim 16$  nm,  $G \sim 24$  nm. (c)  $D_{\text{Au}} \sim 80$  nm,  $D_{\text{Pd}} \sim 16$  nm,  $G \sim 45$  nm. Nominal thickness of all Au nanodisks presented in this figure is 40 nm. The Pd thickness is 10 nm. The blue scattering spectra correspond to the signal obtained with polarization perpendicular to the dimer axis, red curves correspond to the signal obtained with polarization parallel to the dimer axis, and black curves correspond to the unpolarized signal. For the hydrogen sensing measurements, the dotted lines represent the raw signal from the structures and the solid lines are 5 point moving average smoothing as a guide for the eye (red is the measurement with light polarized parallel to dimer axis and blue is the light polarized perpendicular to dimer axis). The area with no shading corresponds to 0.3% H<sub>2</sub> concentration and the yellow shaded area corresponds to 15% H<sub>2</sub> concentration. The scale bar in all SEM images is 100 nm.

smaller Pd particle that can absorb hydrogen and forms a hydride,  $\text{PdH}_{x,y}$  above a critical hydrogen pressure.<sup>28</sup> The hydrogen sorption and hydride formation in the Pd antenna element changes its dielectric properties as well as its volume. This is “sensed” by the Au element and gives rise to a spectral shift of its LSPR that we read off.<sup>30,31,42</sup> The above holds true provided that light polarization is parallel to the antenna axis and the Pd particle is localized inside the near-field of the Au particle, giving rise to mutual coupling (blue spectra in the inset of Figure 5). However, if the light polarization is perpendicular to the antenna axis (red spectra in the inset of Figure 5), the Pd particle is located outside the Au element’s near-field (no coupling) and no spectral shift of the LSPR occurs upon hydride formation. This becomes even clearer from the main graph in Figure 5. It shows the response from our sensor obtained by using a polarizing beam splitter (for details we refer to the Methods section) to read out the spectral position of the LSPR for both polarizations simultaneously. The sample is initially immersed in pure Ar gas at 30 °C. After ca. 4 min, 4% H<sub>2</sub> gas in Ar is introduced (yellow shaded area in Figure 5). Upon hydride formation in the Pd element a spectral blue shift of the parallel LSPR peak is observed, whereas no shift occurs for the resonance perpendicular to the antenna axis. As we change back to pure Ar, the observed shift of the parallel resonance is completely reversed, as expected. This simple test very nicely highlights two key features of our approach: (i) It illustrates the high quality of our fabricated structures at a macroscopic level, that is, how homogeneous and well-oriented the antennas and constituting elements are at the mm<sup>2</sup> level. (ii) It confirms that the intrinsic material properties of the antenna elements are unaffected by the fabrication, that is, that Pd is still catalytically active toward hydrogen dissociation on its surface (no contamination) and forms a bulk hydride phase.

In our second example, we again employ hydrogen sensing as our model system. However, this time at the single particle level and using dark-field scattering spectroscopy (DFSS). We focus on structures that consist of Au nanodisk dimers with a small Pd nanoparticle deposited in the dimer gap by using the Cr funnel approach. We use three dimer structures fabricated with slightly different geometry: 34 nm gap with 26 nm Pd particle (Figure 6a), 24 nm gap with 16 nm Pd particle (Figure 6b), and 45 nm gap with 16 nm Pd particle (Figure 6c). A control measurement without Pd in the gap is shown in Supporting Information Figure S5. For each structure, we provide polarization-dependent scattering spectra and monitor hydride formation and decomposition in situ. Similar to the previous example with ensemble measurements, we flush H<sub>2</sub> gas in and out of the system and use Ar as carrier gas. First, the structures are exposed to 0.3% H<sub>2</sub> in Ar at 30 °C, and after 5 min 15% H<sub>2</sub> gas in Ar is introduced (yellow shaded area in Figure 6). For all three structures, we follow the changes in peak position using light polarized parallel to the dimer axis (red curve) and perpendicular to it (blue curve). As can be seen from Figure 6, the signal from the parallel polarization gives significantly larger shifts in peak position, and also the shifts are larger for the larger Pd particle size and smallest (i.e., basically absent) for the largest gap size (Figure 6c). These trends clearly indicate the importance of the hot spot created by the Au dimer antenna (larger near-field enhancement for smaller gap<sup>2,3</sup>) for the detection of the hydride formation in these very small Pd nanoparticles. Normalized by Pd volume in the hot spot our dimer-based hydrogen sensors yield 1 order of magnitude higher sensitivity in comparison with the tailored nanofocus presented by Liu et al.<sup>10</sup> The detailed calculation is presented in the Supporting Information. Moreover, they also demonstrate the unique opportunities offered by SHCL to engineer and optimize such effects with high accuracy due to the inherent

self-alignment of the approach. We also note that the reason for the nonperfect polarization dependence of the shown measurements (compared to the ensemble example above) most likely is due to the fact that without a “blocker” of the type introduced by Brown et al.<sup>43</sup> the light polarization in our DFSS setup is not perfect because illumination from all directions occurs. Finally, we comment on the reason for the observed difference in terms of spectral response (blue versus red shift) observed upon hydride formation in the Pd particle for the two different antenna types used in the ensemble and single particle measurements, respectively. As shown by Tittl et al.,<sup>42</sup> the reason is related to a compensation effect between the dielectric changes (inducing spectral blue shift) and the volume increase of the Pd upon hydrogen sorption (inducing spectral red shift). Thus, depending on the specifics of the Au–Pd particle arrangement and respective sizes and shapes, it is possible that the effective peak shift is to the blue or to the red (or even zero).

In conclusion, by exploiting the effect of a “shrinking hole” during material deposition through a hole-mask prepared by a colloidal lithography process, we have demonstrated three versatile and self-aligned nanofabrication strategies. They allow the efficient fabrication of complex plasmonic nanoantenna structures consisting of several elements, each of which can be tuned with a high level of control in terms of size (sub-10 nm), relative positioning, but also material composition, that is, heteromaterial arrangements are easily possible in a single lithography step. As supported by the various presented examples, the SHCL technique is characterized by high flexibility in terms of exploited materials, absence of contamination after fabrication or alteration of deposited material properties. Moreover, SHCL features the unique possibility to both uniformly pattern large surface areas ( $\text{cm}^2$ ) and prepare surfaces suitable for single particle sensing. Along these lines we have demonstrated the functionality of plasmonic heteromaterial nanoarchitectures made by SHCL by using hydrogen sensing both at ensemble and single particle level as the model system.

We also highlight that the presented novel concepts of exploiting sacrificial nanostructures for the self-aligned transfer and size/position control of small nanoparticles made from different materials to nanoantenna hot spots are generic. This means that also alternative methods that do not rely on colloidal self-assembly, for example, EBL or FIB, equally well can be used to produce the initial mask. Moreover, the presented SHCL nanofabrication strategies are also highly relevant to other areas of surface and nanoscience than nanoplasmonics. For example, we envision unique possibilities for the fabrication of model catalysts where the role of position and interplay of the noble metal catalyst and (oxidic) support via spillover effects could be scrutinized in detail.<sup>44,45</sup>

#### Methods. Hole-Mask Colloidal Lithography Steps 1–9.

The first 9 steps of the standard hole-mask colloidal lithography nanofabrication method<sup>26</sup> used to fabricate the hole-masks further exploited in the new SHCL processing presented above are illustrated in Supporting Information Figure S1 and summarized briefly below with focus on the specific details relevant to this work. All samples were fabricated on either glass (Borofloat, Schott Scandinavia AB), thermally oxidized silicon (oxide thickness 50 nm) or silicon wafers according to the following protocol. (Step 1) Substrates are cleaned with step-by-step sonication in acetone, isopropyl alcohol (IPA), and methanol. (Step 2) Clean substrates are spin-coated with

poly(methyl methacrylate) (PMMA, MicroChem Corporation, 4 wt % diluted in anisole,  $M_W = 950\,000$ ) at 2000 rpm for 1 min, which yields a thickness of PMMA  $\sim 280$  nm. They are then soft baked at 170 °C for 10 min on a hot plate. (Step 3) The substrate with the thin PMMA layer is etched shortly (5 s) in oxygen plasma (50 W, 250 mTorr, Plasma Therm Batchtop RIE 95m) in order to reduce the hydrophobicity of the surface. (Step 4) Water-suspended positively charged polyelectrolyte (poly(diallyldimethylammonium chloride) (PDDA)  $M_W = 200\,000\text{--}350\,000$ , Sigma-Aldrich, 0.2 wt % in Milli-Q water, Millipore) is dispersed on the surface for 40 s. The substrate is then rinsed with deionized water to remove excess PDDA and dried with nitrogen blow. PDDA forms a thin positively charged polyelectrolyte layer on the PMMA surface. (Step 5) A colloidal suspension of negatively charged polystyrene (PS, sulfate latex, Interfacial Dynamics Corporation (sizes of  $80 \pm 4.51$ ,  $110 \pm 4.51$ , and  $140 \pm 5.18$  nm) or MicroParticles GmbH ( $105 \pm 4$  nm)) particles was then deposited on the surface. Electrostatic repulsion between the PS particles and attraction between PS and the PDDA-treated surface, respectively, creates an amorphous (no long-range order) PS nanoparticle array. The PS particles were diluted in Milli-Q water (Millipore) with a concentration of 0.2 wt % for samples used in ensemble measurements and 0.0001 wt % for samples used in single particle measurements. (Step 6) A thin film of a material, which is resistant to reactive oxygen plasma etching (typically Au or Cr), is evaporated to form the mask layer. Here, 20 nm films of either Au or Cr were evaporated at a base pressure of  $5 \times 10^{-7}$  Torr; evaporation rate is 1.5 Å/s in a Lesker PVD 225 Evaporator. (Step 7) After mask deposition, the PS particles were “stripped” away with tape (SWT-10, Nitto Scandinavia AB), leaving nanoholes in the plasma-resistant film layer (“hole-mask”). (Step 8) Reactive oxygen plasma etching (50 W, 250 mTorr, Plasma Therm Batchtop RIE 95m) was applied to selectively remove the exposed PMMA layer below the holes. The etching creates a partial undercut in the PMMA as clearly seen in the corresponding SEM image in Figure 2b and Supporting Information Figure S1f. The depth of the undercut varies with applied etch time and also depends on the size of the PS particles used. (Step 9) At this stage, the processing route of HCL can take different directions in order to achieve various nanostructure shapes.<sup>26</sup> For example, nanodisks can be obtained by simply depositing material through the hole-mask at the normal angle (Supporting Information Figure S1a). Nanocones can conveniently be made if the evaporation is continued until the holes in the mask completely close due to the shrinking of the hole as material is deposited on the rims of the holes (Supporting Information Figure S1b). Nanodisk dimers are obtained by evaporation of the material at two opposite angles ( $\pm\alpha$ ) from the surface normal (Supporting Information Figure S1c). Note that due to the hole shrinking when material is deposited on the edges in this case it will result in uneven size distribution of nanodisks in each pair. In order to have even size of the disks in each pair, the angle of evaporation has to be alternated every 5 nm of deposited material. In this work, the growth of Au or Ag nanodisks was achieved with either resistive (rate 1 Å/s, Edwards 306 Evaporator, Au nanodisks in Figures 1a and 3) or e-beam evaporation (rate 1 Å/s, Lesker PVD 225 Evaporator, Au or Ag nanodisks in all other figures). The small particles observed around some Au nanodisks (e.g., Figures 1a and 3a–h) are Au particles, which are formed most likely due to “splashing” that occurs when evaporated Au atoms/clusters traveling to the sample substrate

collide with the edges of the hole-mask, and therefore slightly change their direction and end up off the main target area determined by the hole-mask. It is a characteristic and inevitable feature in the cases when underetching of the mask is present (also, e.g., when EBL double-layer resists are used), however the effect can be reduced to some extent using e-beam evaporation rather than resistive evaporation.

**SHCL Steps 10–13 for the C Cone Approach.** Deposition of the C nanocones was carried out in an AVAC HVC600 e-beam evaporator at a base pressure of  $\sim 1.5 \times 10^{-6}$  mbar. Carbon strongly outgases during the first heating and tends to increase vacuum pressure in the chamber. Thus, carbon is first heated (for about 10 min) by slowly increasing the current and sweeping e-beam over the source until the chamber pressure reaches  $\sim 9 \times 10^{-6}$  mbar. Then titanium (Ti) is evaporated with evaporation rate 1 Å/s for several minutes in order to decrease the vacuum pressure in the chamber back to base pressure. Then carbon is again slowly heated but without sweeping the beam and evaporated at the rate of 0.5–1 Å/s. The “particle material” (Pd) was then deposited directly after carbon in the same deposition chamber at normal incidence (evaporation rate  $\sim 0.5$  Å/s). Lift-off of the samples was done in acetone. The C cones were removed by oxygen plasma etching for duration of 5 to 8 min (50 W, 250 mTorr, Plasma Therm Batchtop RIE 95m), depending on the cone height (80 to 110 nm).

**SHCL Steps 10–13 for Cr Cone Approach.** Cr cones were deposited at a base pressure of  $5 \times 10^{-7}$  Torr and with a rate of 2 Å/s (Lesker PVD 22S Evaporator). Lift-off of the samples was done in acetone. The Cr cones were removed by dipping sample in Cr etch for 1 min (Sunchem AB, NiCr etchant 65009S, composition: ceric ammonium nitrate 10–15%, nitric acid 15–20%, DI water 60–70%).

**SHCL Steps 10–12 for Cr Funnel Approach.** The Cr funnels were deposited at a base pressure of  $5 \times 10^{-7}$  Torr and with a rate of 2 Å/s (Lesker PVD 22S Evaporator). The tilt angle  $\beta$  was 30°. Rotation speed of the substrate holder was kept at 5 rpm for all samples. The particle material (Pd) was then deposited directly after Cr in the same deposition chamber at normal incidence with nominal thickness of 10 or 20 nm (base pressure  $4 \times 10^{-8}$  Torr, evaporation rate  $\sim 1.5$  Å/s). Lift-off was done in acetone.

**Polarization-Dependent Hydrogen Sensing Measurements.** The nanoantenna structures were fabricated on a glass substrate (borosilicate glass) using the sacrificial Cr cone approach described above. The samples were introduced into a quartz tube gas reactor system (Insplorion X1, Insplorion AB, Göteborg, Sweden), subjected to Ar flow (100 mL/min) and heated to 30 °C. After 10 min in Ar in pulses of 5 min, 4% hydrogen in Ar was introduced into the gas flow in the reactor. The sample is illuminated through the reactor quartz tube using a fiber coupled halogen lamp (AvaLight-Hal-S, Avantes). Optical extinction spectra from the sample are obtained by two fiber-coupled spectrometers (AVASpec-1048, Avantes) via a polarizing beam splitter (CM1-PBS252, Thorlabs) in order to obtain two polarizations at the same time. The spectral peak positions were extracted by fitting the top region ( $\pm 100$  nm from peak position) of the measured LSPR peaks for the respective polarizations with a Lorentzian function. In this range, a good fit to the experimental data could be obtained and yielded a low signal/noise. We note that alternative peak fitting procedures such as using a polynomial or Gaussian function equally well could have been used and may yield slightly different absolute peak shift values. Such details will be

important in future studies where a detailed quantitative comparison in sensing performance between different structure designs or a deeper detailed understanding of the plasmonic properties of the different antennas is sought. This is, however, beyond the scope of this work where we only are interested in the use of hydrogen sensing as a model system to demonstrate what functionality that can be achieved with structures made by SHCL, that is, whether or not the made structures exhibit the targeted hydrogen sensing function. The sample was subjected to several hydrogen pulses and after approximately three cycles a stable signal was obtained. The reason for the initial signal instability/irreversibility is removal of surface contaminations such as water and hydrocarbons from the Pd particle and the sensor structures due to immersion into dry atmosphere. Other contributions stem from the reduction of any surface oxide present on the Pd and/or restructuring in the Pd particle due to the hydrogen-induced expansion of the Pd crystal lattice. Figure 5 above shows the fifth hydrogen pulse to which the sample was subjected.

**Single Particle Dark-Field Scattering Measurements.** The samples used for the single particle measurements were fabricated on a thermally oxidized silicon wafer with oxide thickness of 50 nm using the sacrificial Cr funnel approach. The sample was placed in a quartz cup and put inside a temperature-controlled stage (Linkam, THMS600), which is compatible with our Nikon Eclipse LV100 upright optical microscope. The stage was connected to a set of mass flow controllers (Bronkhorst) that have several different working ranges to supply the desired flow of reactants to the measurement stage. Samples were exposed to 0.3% H<sub>2</sub> and 15% H<sub>2</sub> in Ar carrier gas with time interval of 5 min and flow rate of 140 mL/min. The illumination source of the microscope consists of a 50 W halogen lamp (Nikon LV-HL50W LL). The Rayleigh scattering from individual plasmonic nanostructures was collected using a 50× objective (Nikon 50× BD). For single particle spectroscopy the scattered light was collected by an optical fiber (Ocean Optics, UV-vis 200 μm core) and directed to the entrance slit (500 μm) of a spectrometer (Andor Shamrock SR303i). At magnification of 50×, the estimated sampling area is  $\sim 12.5$  μm<sup>2</sup>, which allows for selective collection of the scattered light from individual nanoantennas fabricated at low density on the sample surface. The collected light was dispersed using a grating (150 lines/mm, blaze wavelength 800 nm). The scattering spectra were recorded using a thermoelectrically cooled CCD camera (Andor Newton). Normalized scattering spectra  $I_{sc}$  from individual nanoantennas were obtained as a function of wavelength  $\lambda$  using the relation  $I_{sc}(\lambda) = (S - D)/CRS$ , where  $S$  is the collected signal from an area with nanoantenna,  $D$  is the signal from the nearby area without nanoantenna (dark signal for background correction), and CRS is the signal collected from the diffuse white certified reflectance standard (Labsphere SRS-99-020). CRS is used in order to correct the signal for the lamp spectrum. The acquisition time for each spectrum was 9 s. Curves that represent polarization-dependent changes of the peak position in time (Figure 6) were obtained by fitting a Lorentzian curve to the top region ( $\pm 100$  nm from peak position) of the raw scattering spectra.

## ASSOCIATED CONTENT

### Supporting Information

Description of HCL steps, estimation of nanostructure dimensions for each fabrication approach, details of single particle DFSS measurements, and overview SEM images of

nanostructure arrays at low magnification. This material is available free of charge via the Internet at <http://pubs.acs.org>.

## AUTHOR INFORMATION

### Corresponding Author

\*E-mail: clangham@chalmers.se.

### Author Contributions

The manuscript was written through contributions of all authors. All authors have given approval to the final version of the manuscript.

S.S. and C.W. contributed equally.

### Notes

The authors declare no competing financial interest.

## ACKNOWLEDGMENTS

We acknowledge financial support from the Swedish Research Council Project 2010-4041, the Swedish Foundation for Strategic Research Framework Program RMA11-0037, the Chalmers Area of Advance for Nanoscience and Nanotechnology, and the Knut and Alice Wallenberg Foundation for their support of the  $\mu$ -fab cleanroom infrastructure in Sweden.

## REFERENCES

- (1) Novotny, L.; van Hulst, N. *Nat. Photonics* **2011**, *5*, 83–90.
- (2) Hao, E.; Schatz, G. C. *J. Chem. Phys.* **2004**, *120*, 357–366.
- (3) Halas, N. J.; Lal, S.; Chang, W.-S.; Link, S.; Nordlander, P. *Chem. Rev.* **2011**, *111*, 3913–3961.
- (4) Muhschlegel, P.; Eisler, H. J.; Martin, O. J. F.; Hecht, B.; Pohl, D. W. *Science* **2005**, *308*, 1607–1609.
- (5) Larsson, E.; Syrenova, S.; Langhammer, C. *Nanophotonics* **2012**, *1*, 249.
- (6) Larsson, E. M.; Langhammer, C.; Zorić, I.; Kasemo, B. *Science* **2009**, *326*, 1091–1094.
- (7) Linic, S.; Christopher, P.; Ingram, D. B. *Nat. Mater.* **2011**, *10*, 911–921.
- (8) Christopher, P.; Xin, H. L.; Marimuthu, A.; Linic, S. *Nat. Mater.* **2012**, *11*, 1044–1050.
- (9) Mubeen, S.; Lee, J.; Singh, N.; Kramer, S.; Stucky, G. D.; Moskovits, M. *Nat. Nanotechnol.* **2013**, *8*, 247–251.
- (10) Liu, N.; Tang, M. L.; Hentschel, M.; Giessen, H.; Alivisatos, A. P. *Nat. Mater.* **2011**, *10*, 631–636.
- (11) Liu, N.; Wen, F.; Zhao, Y.; Wang, Y.; Nordlander, P.; Halas, N. J.; Alù, A. *Nano Lett.* **2012**, *13*, 142–147.
- (12) Schnell, M.; Garcia-Etxarri, A.; Huber, A. J.; Crozier, K.; Aizpurua, J.; Hillenbrand, R. *Nat. Photonics* **2009**, *3*, 287–291.
- (13) Kinkhabwala, A.; Yu, Z. F.; Fan, S. H.; Avlasevich, Y.; Mullen, K.; Moerner, W. E. *Nat. Photonics* **2009**, *3*, 654–657.
- (14) Roxworthy, B. J.; Ko, K. D.; Kumar, A.; Fung, K. H.; Chow, E. K. C.; Liu, G. L.; Fang, N. X.; Toussaint, K. C. *Nano Lett.* **2012**, *12*, 796–801.
- (15) Farahani, J. N.; Pohl, D. W.; Eisler, H. J.; Hecht, B. *Phys. Rev. Lett.* **2005**, *95*, 017402.
- (16) Kang, J.-H.; Kim, K.; Ee, H.-S.; Lee, Y.-H.; Yoon, T.-Y.; Seo, M.-K.; Park, H.-G. *Nat. Commun.* **2011**, *2*, 582.
- (17) Wissert, M. D.; Schell, A. W.; Ilin, K. S.; Siegel, M.; Eisler, H. J. *Nanotechnology* **2009**, *20*, 425203.
- (18) Ahmed, A.; Gordon, R. *Nano Lett.* **2011**, *11*, 1800–1803.
- (19) Grigorenko, A. N.; Roberts, N. W.; Dickinson, M. R.; Zhang, Y. *Nat. Photonics* **2008**, *2*, 365–370.
- (20) Jain, P. K.; Huang, W.; El-Sayed, M. A. *Nano Lett.* **2007**, *7*, 2080–2088.
- (21) Ueno, K.; Juodkazis, S.; Shibuya, T.; Yokota, Y.; Mizeikis, V.; Sasaki, K.; Misawa, H. *J. Am. Chem. Soc.* **2008**, *130*, 6928–6929.
- (22) Tsai, C. Y.; Lin, J. W.; Wu, C. Y.; Lin, P. T.; Lu, T. W.; Lee, P. T. *Nano Lett.* **2012**, *12*, 1648–1654.
- (23) Near, R.; Tabor, C.; Duan, J.; Pachter, R.; El-Sayed, M. *Nano Lett.* **2012**, *12*, 2158–2164.
- (24) Lesuffleur, A.; Kumar, L. K. S.; Brolo, A. G.; Kavanagh, K. L.; Gordon, R. *J. Phys. Chem. C* **2007**, *111*, 2347–2350.
- (25) Huang, C. P.; Zhang, Y.; Wang, Q. J.; Yin, X. G.; Wang, G. D.; Liu, J. Q.; Zhu, Y. Y. *J. Phys. Chem. C* **2011**, *115*, 24621–24626.
- (26) Fredriksson, H.; Alaverdyan, Y.; Dmitriev, A.; Langhammer, C.; Sutherland, D. S.; Zaech, M.; Kasemo, B. *Adv. Mater.* **2007**, *19*, 4297–4302.
- (27) Yang, S.-M.; Jang, S. G.; Choi, D.-G.; Kim, S.; Yu, H. K. *Small* **2006**, *2*, 458–475.
- (28) Fukai, Y. *The Metal-Hydrogen System*; Springer-Verlag: Berlin, 1993.
- (29) Langhammer, C.; Zorić, I.; Kasemo, B.; Clemens, B. M. *Nano Lett.* **2007**, *7*, 3122–3127.
- (30) Zoric, I.; Larsson, E. M.; Kasemo, B.; Langhammer, C. *Adv. Mater.* **2010**, *22*, 4628–4633.
- (31) Ameen Poyli, M.; Silkin, V. M.; Chernov, I. P.; Echenique, P. M.; Diez Muino, R.; Aizpurua, J. *J. Phys. Chem. Lett.* **2012**, *3*, 2556–2561.
- (32) Langhammer, C.; Larsson, E. M.; Zhdanov, V. P.; Zorić, I. *J. Phys. Chem. C* **2012**, *116*, 21201–21207.
- (33) Langhammer, C.; Larsson, E. M.; Kasemo, B.; Zorić, I. *Nano Lett.* **2010**, *10*, 3529–3538.
- (34) Langhammer, C.; Zhdanov, V. P.; Zorić, I.; Kasemo, B. *Chem. Phys. Lett.* **2010**, *488*, 62–66.
- (35) Langhammer, C.; Zhdanov, V. P.; Zorić, I.; Kasemo, B. *Phys. Rev. Lett.* **2010**, *104*, 135502.
- (36) Tang, M. L.; Liu, N.; Dionne, J. A.; Alivisatos, A. P. *J. Am. Chem. Soc.* **2011**, *133*, 13220–13223.
- (37) Shegai, T.; Langhammer, C. *Adv. Mater.* **2011**, *23*, 4409–.
- (38) Tittl, A.; Yin, X.; Giessen, H.; Tian, X.-D.; Tian, Z.-Q.; Kremers, C.; Chigrin, D. N.; Liu, N. *Nano Lett.* **2013**, *13*, 1816–1821.
- (39) Li, K.; Stockman, M. I.; Bergman, D. J. *Phys. Rev. Lett.* **2003**, *91*, 227402.
- (40) Bidault, S.; García de Abajo, F. J.; Polman, A. *J. Am. Chem. Soc.* **2008**, *130*, 2750–2751.
- (41) Höppener, C.; Lapin, Z. J.; Bharadwaj, P.; Novotny, L. *Phys. Rev. Lett.* **2012**, *109*, 017402.
- (42) Tittl, A.; Kremers, C.; Dorfmüller, J.; Chigrin, D. N.; Giessen, H. *Opt. Mater. Express* **2012**, *2*, 111–118.
- (43) Brown, L. V.; Sobhani, H.; Lassiter, J. B.; Nordlander, P.; Halas, N. J. *ACS Nano* **2010**, *4*, 819–832.
- (44) Johánek, V.; Laurin, M.; Grant, A. W.; Kasemo, B.; Henry, C. R.; Libuda, J. *Science* **2004**, *304*, 1639–1644.
- (45) Cargnello, M.; Jaén, J. J. D.; Garrido, J. C. H.; Bakmutsky, K.; Montini, T.; Gámez, J. J. C.; Gorte, R. J.; Fornasiero, P. *Science* **2012**, *337*, 713–717.